Dalton Transactions

ROYAL SOCIETY OF CHEMISTRY

PAPER

View Article Online
View Journal | View Issue

Cite this: *Dalton Trans.*, 2024, **53**, 6224

Phonon softening induced phase transition of $CeSiO_4$: a density functional theory study†

Xiaodong Zhao,[a] Andrew C. Strzelecki,[b,c] Nicolas Dacheux,[d] Liang Qi*[e] and Xiaofeng Guo*[a,b]

Received 20th January 2024,
Accepted 10th March 2024

DOI: 10.1039/d4dt00179f

rsc.li/dalton

Density functional theory plus Hubbard U (DFT+*U*) methodology was used to calculate the structures and energetic landscapes of $CeSiO_4$, including its stetindite and scheelite phases from ambient pressure to ~24 GPa. To ensure accurate simulations of the high-pressure structures, assessments of strain–stress methods and stress–strain methods were conducted in prior, with the former found to have a better agreement with the experimental result. From DFT calculations the equation of states (EOS) of both stetindite and scheelite were further obtained, with the fitted bulk moduli being 182(2) GPa and 190.0(12) GPa, respectively. These results were found to be consistent with the experimental values of 177(5) GPa and 222(40) GPa. Furthermore, the calculated energetics suggest that the stetindite structure is more thermodynamically stable than the scheelite structure at a pressure lower than 8.35 GPa. However, the stetindite → scheelite phase transition was observed experimentally at a much higher pressure of ~15 GPa. A further phonon spectra investigation by the density functional perturbation theory (DFPT) indicated the E_g^1 mode is being softened with pressure and becomes imaginary after 12 GPa, which is a sign of the lattice instability. Consequently, it was concluded that the stetindite → scheelite transition is predominantly initiated by the lattice instability under high-pressure.

1. Introduction

Minor actinides in radioactive waste, including neptunium (Np), plutonium (Pu), americium (Am) and curium (Cm), pose substantial challenges in terms of their long-term management and secure disposal due to their long half-life, high radiotoxicity and biotoxicty.[1–3] In the United States, there are two primary resources of actinide radioactive waste: (*i*) the spent nuclear fuel (SNF) from nuclear power plants (NPPs). Typical nuclear power plant (NPP) generating ~1 GW-e per year produces ~25 tonnes of SNF.[4] The US is following a 'once-through' processing policy, which means the residue uranium (U), Pu and other minor actinides are not reprocessed and retried from the SNF, all these actinides will be solidified and directly disposed in the future deep geological site. In countries with reprocessing and nuclear fuel cycle policies, like France, the PUREX process is utilized, in which U and Pu are extracted, and minor actinides from the 1st cycle 1AW raffinate are vitrificated and will be disposed in deep geological site;[5] (*ii*) the significant accumulation of plutonium by the US nuclear weapon program from World War II to cold war.[6] The weapon grade plutonium does not only raise environmental issues but also non-proliferation concerns.[7–9] It is crucial to safely dispose the radioactive waste and isolate them out of any biospheres. Various forms, including glasses, ceramics, and glass-ceramics forms have been proposed to enclose the spent nuclear fuel or high-level waste (HLW).[10,11] Among them, ceramic form has been highly recommended for actinide immobilization, especially the fluorite-related structure (cubic zirconia, pyrochlore, zircon, murataite *etc.*).[4] Actinide orthosilicates ($AnSiO_4$, where An = Th–Am),[12,13] possessing the zircon structure (space group $I4_1/amd$, as in Fig. 1), have emerged as a promising candidate matrix for immobilizing minor actinides due to its remarkable attributes, such as minimal chemical reactivity, low solubility, and robust resistance to radiation-induced damage.[2,14–17] Additionally, aside from its role as a nuclear waste disposal matrix, zircon-structured phase is also being considered as an alteration form during the long-term nuclear waste storage.[18] Most actinide nuclei and the decay daughter nuclei have long half-lives, such

[a]*Department of Chemistry, Washington State University, Pullman, Washington, 99164, USA. E-mail: x.guo@wsu.edu*
[b]*School of Mechanical and Materials Engineering, Washington State University, Pullman, Washington, 99164, USA*
[c]*Earth and Environmental Sciences Division, Los Alamos National Laboratory, Los Alamos, New Mexico, 87545, USA*
[d]*ICSM, Univ Montpellier, CNRS, CEA, ENSCM, Site de Marcoule, Bagnols sur Cèze, 30207, France*
[e]*Department of Materials Science and Engineering, University of Michigan, Ann Arbor, Michigan, 48109, USA. E-mail: qiliang@umich.edu*
† Electronic supplementary information (ESI) available. See DOI: https://doi.org/10.1039/d4dt00179f

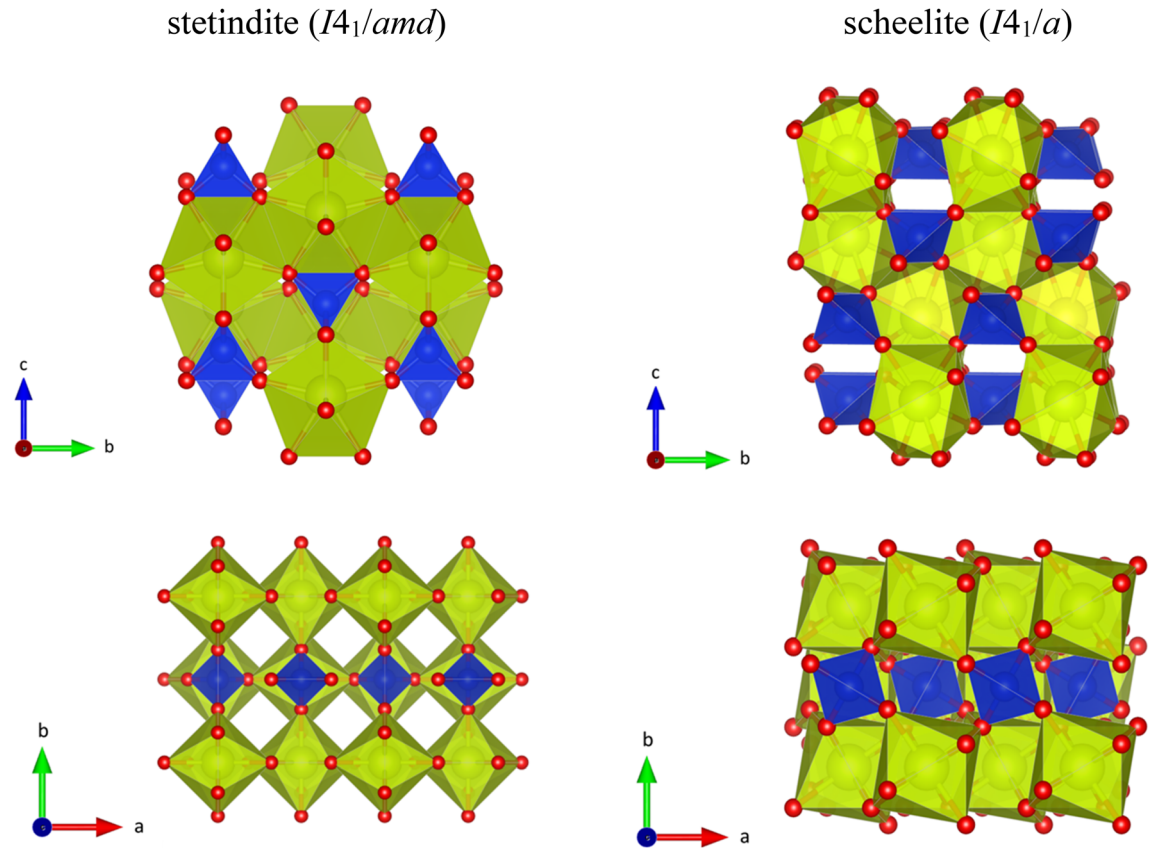

Fig. 1 Crystal structures of the stetindite phase ($I4_1/amd$), and the high-pressure scheelite phase ($I4_1/a$). The yellow polyhedral is the octahedron from Ce–O and the blue polyhedral is the tetrahedron from Si–O. In the stetindite phase, the Ce–O octahedron is sharing edges with the Si–O tetrahedra, while in the scheelite phase, the Ce–O octahedron is sharing corners with the Si–O tetrahedra.

as $T_{1/2,\ Pu\text{-}241}$ = 14.4 years and its second daughter nuclei $T_{1/2,\ Np\text{-}237}$ = 2.1 million years.[19] In such a long timescale, minor actinides in the deep geological site may be leached from the host matrix and in contact with the silica in the back-filled clay and geological barrier of granite, hence could trigger the formation of zircon. It is also evidenced that zircon-structured phases have been found in the nuclear accident sites,[1,20–23] from the high temperature-pressure reaction of actinides with the natural abundant silica-minerals (*e.g.* quartz). To ensure the secure nuclear waste disposal over extended periods, it is essential to understand its stability, structural behavior, and transformation mechanisms under extreme conditions.[24]

More recently, DFT calculation revealed that the phase transformation mechanism of coffinite ($USiO_4$) is governed by both the thermodynamic and lattice instability factors: formation enthalpy of the scheelite-type $USiO_4$ becomes lower than that of the coffinite phase at around 16 GPa (ref. 25) and the B_{2u} silent mode becomes imaginary at around 12.5 GPa (ref. 26) aligning well with the experimental phase transition pressure observed at around 15 GPa.[25] However, there is less research on $CeSiO_4$ stetindite, on the theoretical side,[27,28] with only one study present in the literature.[29] To date, there is also only one experimental study of $CeSiO_4$ under high pressure.[30] In practice, stetindite ($CeSiO_4$) can be served as a suitable analogue[17,31] to $PuSiO_4$ due to the inherent challenges associated with handling radioactive plutonium and synthetic challenges to acquire pure phase of $PuSiO_4$, as cerium carries both +3 and +4 charges and exhibits similar ionic radii to plutonium, allows for more manageable experimentation.[32–35] *In situ* high-pressure Raman spectroscopy experiments and synchrotron X-ray diffraction have revealed that phase transition of stetindite differs from coffinite. Stetindite undergoes a phase transition to a newly characterized high-pressure low-symmetry (HPLS) polymorph (space group: $I\bar{4}_2d$) at approximately 15 GPa.[30] This transition results from slight rotational and torsional adjustments in the SiO_4 and MO_8 polyhedral within the zircon structure.[36] Further compression to 18 GPa leads to a transition to a scheelite structure type (space group: $I4_1/a$, as in Fig. 1).[30] However, a fundamental question remains unanswered: is the phase transition governed by enthalpy or lattice instabilities or both of them?

This paper extends the scope of lattice dynamics studies and provides a comprehensive analysis of the phonon spectra phases, with a specific focus on the properties of the soft mode. Employing first-principles calculations, we investigated the structural and dynamic properties during the phase transition from stetindite to scheelite. Pressure was applied using a strain–stress method, and phonon–dispersion curves were

obtained through density functional perturbation theory (DFPT) methodology. The calculation methods are presented in the Methodology section. The external pressure simulation and crystal structural evolution under varying pressures, with their corresponding phonon dispersion curves can be found in the Results and discussion section.

2. Methodology

Periodic DFT+*U* calculations were performed by using Vienna *Ab initio* Simulation Package (VASP) 5.4.4.[37–40] Generalized gradient approximation (GGA) was used for the exchange–correlation function, and projector-augment wave (PAW) pseudopotentials were used for the core electrons.[41,42] GW-PAW potentials was selected based on initial testing with various pseudopotentials. This pseudopotential with GW approximation, introduced by VASP, can be applicable in both DFT and GW calculations to deliver highly accurate results. The selection of GW-PAW potentials demonstrated a volume discrepancy of merely 2% to 2.5% compared with experimental data, which is well within the acceptable error range for DFT calculations in the VASP framework. The valence electrons of cerium, silicon, and oxygen were respectively set as $5s^2 5p^6 4f^1 5d^1 6s^2$, $2s^2 2p^6 3s^2 3p^2$, and $2s^2 2p^4$. The 2s electrons of silicon were also regarded as valence electrons. Cutoff energy was set to be 700 eV, and this high energy cutoff value is more computationally expensive, but it ensured the accuracy to represent the role of electrons under high pressure. The strong on-site repulsion force of highly localized cesium 4f electrons necessarily needs to be considered in the compacted high-P structure, hence an effective Hubbard *U* of 4.0 eV was set for 4f electron.[43] In ionic and electronic optimization steps, total energy was converged to 1×10^{-5} eV and force between ions was converged to 1×10^{-4} eV Å^{-1}. Sampling mesh in Brillion zone was set to be $7 \times 7 \times 7$ based on convergence study. All the calculations were performed at nearly 0 K, and the acquired lattice constants and enthalpy maybe different with measured results in experiments. The thermal expansion at high temperate, and anharmonic vibrational behavior could all make the measured lattice constant different from DFT+*U* results. The approximation in the treatment of electron–electron interaction (*e.g.* exchange–correlation functional) and neglection of zero-point vibrations at 0 K will also make the computed enthalpy values be a bit different with the real case. In this work, DFT results are always compared with available experimental results, and also make complement to the experiments by providing insights which is hard to be measured, such as the thermodynamic properties at high-pressure.

The density functional perturbation theory (DFPT) in the harmonic approximation in the PHONOPY package was applied to compute the phonon modes.[44–47] DFPT is a methodology that builds upon DFT, which perturbs the atomic positions from their equilibrium positions along symmetry-unique directions.[44] The energy and restoring force are calculated employing VASP and are used for subsequent processing in PHONOPY for calculations of corresponding force constants. A $2 \times 1 \times 1$ supercell was used throughout the calculations to avoid unphysical self-interaction of the perturbated atoms due to the periodic conditions. Only the vibrations at the Γ-point of the Brillouin (*i.e.*, $q = 0$) was considered for the assignment of irreducible representations to each mode at the center of the Brillouin zone according to the character table of the underlying point group which the structure belongs to, *i.e.* D_{4h} ($4/mmm$) for zircon.[48] And the eigenmodes were assigned by the comparison based on previous research of $ZrSiO_4$ and $USiO_4$ at ambient condition.[25,26,49,50]

To apply an external hydrostatic force to the system, two computational techniques can be used. The first method is the strain–stress approach, where lattice parameters are adjusted, and the induced Hellmann–Feynman force serves as the hydrostatic force.[51,52] To create a uniaxial hydrostatic pressure by strain–stress method, the strain tensor needs to be diagonal. A new unit cell is built upon a hydrostatic pressure as eqn (1):

$$\begin{aligned} A' = A \cdot \varepsilon_{ij} &= \begin{bmatrix} a & 0 & 0 \\ 0 & a & 0 \\ 0 & 0 & c \end{bmatrix} \begin{bmatrix} 1-\delta & 0 & 0 \\ 0 & 1-\delta & 0 \\ 0 & 0 & 1-\delta' \end{bmatrix} \\ &= \begin{bmatrix} (1-\delta)\cdot a & 0 & 0 \\ 0 & (1-\delta)\cdot a & 0 \\ 0 & 0 & (1-\delta')\cdot c \end{bmatrix} \end{aligned} \quad (1)$$

where A' and A matrix contain the cell lattice vectors in Cartesian form, ε_{ij} is the diagonal strain tensor.[53]

Besides the diagonal components, all the other values in the strain tensor are kept as zero to eliminate the shear stress. The stress force is calculated by the first derivatives of energy with respect to the strain by eqn (2),

$$\sigma_{ij} = \frac{1}{V}\frac{\partial E}{\partial \varepsilon_{ij}} \quad (2)$$

where E is energy, and the σ_{ij} is the stress tensor.

In VASP 5.4.4, the stress tensor is computed following the Fellman–Feynman theorem[52,54] and can be directly read from the output files by the convention of σ_i, where i runs from 1–6 following the notation of *xx*, *yy*, *zz*, *yz*, *xz*, *xy*.[55] Hence, in VASP 5.4.4, the stress tensor can be expressed as eqn (3):

$$\begin{bmatrix} \sigma_{11} & \sigma_{12} & \sigma_{13} \\ \sigma_{12} & \sigma_{22} & \sigma_{23} \\ \sigma_{13} & \sigma_{23} & \sigma_{33} \end{bmatrix} = \begin{bmatrix} \sigma_1 & \sigma_6 & \sigma_5 \\ \sigma_6 & \sigma_2 & \sigma_4 \\ \sigma_5 & \sigma_4 & \sigma_3 \end{bmatrix} = \begin{bmatrix} \sigma_{xx} & \sigma_{xy} & \sigma_{xz} \\ \sigma_{xy} & \sigma_{yy} & \sigma_{yz} \\ \sigma_{xz} & \sigma_{yz} & \sigma_{zz} \end{bmatrix} \quad (3)$$

In all the calculations, by adjusting the external strain δ and δ' in eqn (1), only the diagonal components of the stress tensor σ_{xx}, σ_{yy} and σ_{zz} are kept-non-zero, and the difference of each stress is within 1%. The final hydrostatic pressure scalar is obtained as the trace of the matrix divided by three, as shown in eqn (4):

$$P = \mathrm{tr}(\sigma_{ij})/3 \quad (4)$$

Hence the calculation of the diagonal stress tensor makes the pressure P and the enthalpy $H = E + PV$ accessible.[56] The unit cell was systematically compressed and expanded, with identical structures from both methods and further confirmed by the material's consistent return to equilibrium positions after random atomic perturbations (Fig. S1†).

The second method is the stress–strain approach, which employs Pulay stress to affect the system, permitting volume relaxation. To ensure the accuracy of the Pulay stress-relaxed structure, a secondary relaxation of the lattice was carried out, followed by energy calculations using the tetrahedron method (the whole flow-chart is shown in Fig. S2†).[54]

3. Results and discussion

3.1 High-pressure structures and enthalpies

A comparison of these two methodologies was conducted to assess the precision of both the strain–stress and stress–strain methods and is shown in Fig. S3.† It is shown that the strain–stress method better approximates the experimental volumes under high pressure, despite minor disparities between the two methods. The simulation also extends the stetindite structure beyond the phase transition at approximately 10 GPa, after which the stetindite phase is not trackable by experiments. This enables us to investigate the underlying mechanism of stetindite being unstable beyond 10 GPa. Nevertheless, a noticeable discrepancy emerges in the energy calculation of about 70 kJ mol^{-1}. Considering the strain–stress method is more accurate in the structural aspect, the enthalpy values derived from the strain–stress method was chosen for further analysis. Enthalpy values are determined by $H = U + PV$, and the results from both methods exhibit substantial similarity. Internal energy values encompass energies from the eigenvalues of the static Schrodinger equation, incorporating potential energy components such as electrostatic (alpha Z and Ewald energy), Hartree, and exchange–correlation energies.[57] The external work is calculated as $P \times V$, with P derived from the generated Hellmann–Feynman force or set Pulay stress.

After the tests, the strain–stress method was selected due to its high accuracy. The computed unit cell parameters and enthalpy values for stetindite and scheelite are summarized in Tables 1 and 2, respectively. The pressure dependence of computed unit cell volumes for two $CeSiO_4$ phases, in comparison with experimental values, were shown in Fig. S3.† Both the experimental and simulated values were fitted using the second-order Birch–Murnaghan equation of state (BMEOS), as shown in the eqn (5) below:[58]

$$P = \frac{3K_0}{2}\left[\left(\frac{V_0}{V}\right)^{\frac{7}{3}} - \left(\frac{V_0}{V}\right)^{\frac{5}{3}}\right] \quad (5)$$

Here V_0 represents the zero-pressure unit cell volume, V is the cell volume at a given pressure (P), and K_0 denotes the bulk modulus. The fits were carried out using the EosFit7 software, which offers the option to incorporate the uncertainties of the data points in the fitting process.[59]

The DFT calculations for stetindite produced EOS closely matching the experimental values, as the calculated zero-pressure unit cell volume and bulk modulus for stetindite are 306.1(2) Å^3 and 182(2) GPa, respectively, consistent with the experimental values of 300.4(2) Å^3 and 177(5) GPa. The fitted curve also displayed similar convergence, affirming the agreement. Conversely, the calculations for scheelite yielded a zero-pressure unit cell volume of 277.5(10) Å^3 and a bulk modulus of 190.0(12) GPa. The EOS fitting for the calculated values differ slightly from the experimental ones, which are 276(3) Å^3 and 222(40) GPa. The bulk modulus from the experimental results fitting is larger than the fitted result from the calculations, also carrying a larger error, which could be due to the scattered nature of the experimental data at high-pressure ranges. These can be seen from the divergence difference between the fitted curves for scheelite based on the calculated and experimental results.

The calculated enthalpy results are presented in Fig. 2(B). The difference in enthalpy suggests that scheelite is the energetically more favorable phase under high pressure, with the phase transition pressure around 8.35 GPa (lower than the experimental value[30]). Even scheelite is more thermodynamic stable above 8.35 GPa, but this phase was not observed during the experiment. It is therefore hypothesized that there are two possible reasons for the difference in transitional pressure: (*i*) the activation energy barrier of the transition is higher than the enthalpy difference between stetindite and scheelite, and thus it requires higher pressure to surpass, (*ii*) the stetindite phase above 8.35 GPa could be thermodynamically metastable

Table 1 Unit cell parameters and enthalpy values of stetindite under high pressures up to ~24 GPa

Simulated pressure/ GPa	a/Å	c/Å	Volume/ Å^3	Enthalpy/ kJ mol^{-1}
−0.23	7.06	6.27	312.52	−4750.34
4.11	6.98	6.24	304.19	−4548.21
8.37	6.92	6.21	297.30	−4354.78
12.45	6.87	6.18	291.39	−4173.61
16.05	6.82	6.16	286.76	−4016.59
19.88	6.78	6.13	282.21	−3852.28
23.98	6.74	6.11	277.74	−3678.80

Table 2 Unit cell parameters and enthalpy values of scheelite under high pressures up to ~24 GPa

Simulated pressure/ GPa	a/Å	c/Å	Volume/ Å^3	Enthalpy/ kJ mol^{-1}
0.09	4.95	11.22	274.61	−4696.45
3.57	4.92	11.12	269.49	−4551.13
7.55	4.90	11.02	264.40	−4388.18
12.44	4.86	10.95	258.91	−4191.90
15.87	4.84	10.88	255.33	−4056.79
20.08	4.82	10.82	251.27	−3893.52
23.94	4.80	10.75	247.80	−3746.39

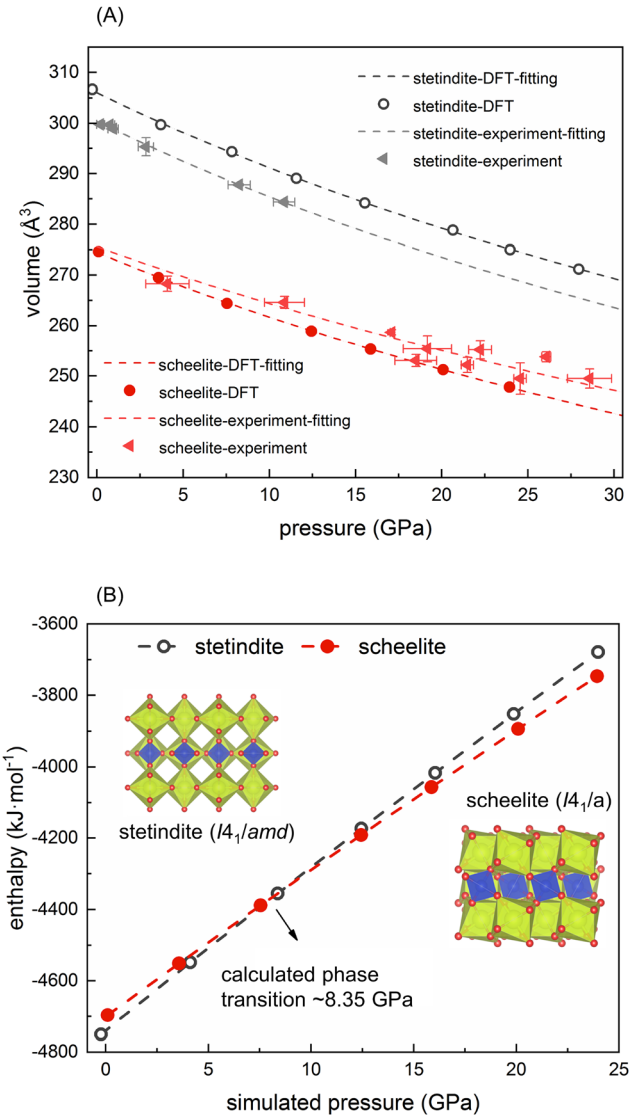

Fig. 2 (A) Pressure–volume relationships of $CeSiO_4$ stetindite and scheelite $CeSiO_4$. The dashed lines are fitting results by the second-order Birch-Murnaghan EOS fitting. Gray or red circle symbols are the results from DFT calculations, and gray or red triangle symbols are experimental values from Rietveld refinement of synchrotron XRD.[30] The experimental data owns some statistical tolerance from the refinements, and the DFT approach is a deterministic approach, hence has no statistical errors. (B) Enthalpic landscape of stetindite and scheelite $CeSiO_4$.

but kinetically stable, so the stetindite structure can be retained to a certain extent in pressure during experiment. Thirty random perturbation tests were conducted to test the hypothesis. The atoms are randomly perturbated by −0.1–0.1 Å from its equilibrium position under 8 GPa, and it was found the atoms relaxed back to the original position all the time. The perturbation result indicated the stetindite structure may be dynamically stable, otherwise the atoms could not remain in place. On the other hand, this random perturbation was also intended to initially test if the phase transition could be a first-order phase transition, which process stochastically displaced atoms and the redistribution of atoms. However, by thirty random displacements, the structure maintained, which is consistent with the observation of an HPLS phase in the experiment that indicates a second-order phase transition or a diffusional transformation. Overall, the enthalpy cross-check point between stetindite and scheelite occurs at around 8.35 GPa, indicating that the scheelite phase is thermodynamically more stable than the stetindite phase beyond this pressure. However, the absence of a phase transition at this pressure suggests that it is not enthalpically driven and may involve lattice dynamics. Further evaluation of the phonon spectrum was conducted to gain a better understanding of the lattice dynamics.

3.2 High-pressure phonon spectra

The phonon spectra are displayed in Fig. 3, which arise from the 12 atoms within the primitive cell and give rise to a total of 36 vibration modes, encompassing 3 acoustic modes and 33 optical modes. The normal modes for stetindite (belonging to space group $I4_1/amd$, point group D_{4h}) can be represented as follows:

$$\Gamma_{\text{acoustic}} = \mathrm{E_u} + \mathrm{A_{2u}} \tag{6}$$

$$\Gamma_{\text{optic}} = 2\mathrm{A_{1g}} + \mathrm{A_{2g}} + \mathrm{A_{1u}} + 3\mathrm{A_{2u}} + 4\mathrm{B_{1g}} + \mathrm{B_{2g}} + \mathrm{B_{1u}} + 2\mathrm{B_{2u}} + 4\mathrm{E_u} + 5\mathrm{E_g} \tag{7}$$

The frequency-wavenumber dispersion curves were calculated through the high symmetry path Γ–X–P–Γ–M–N, which are respectively representing the points of Γ (0, 0, 0), X (0, 0, 1/2), P (1/4, 1/4, 1/4), M (−1/2, 1/2, 1/2) and N (0, 1/2, 0).[50] There are roughly two ranges in the curves, which are corresponding to the Ce–O motions (0 to ~17.5 THz) and Si–O motions (25 THz to 32 THz). The lowest three ones are the three lattice waves. This energy range agreed with previous calculations with zircon $ZrSiO_4$, thorite $ThSiO_4$ and coffinite $USiO_4$.[26,49,58,60–62] Given the isostructural fact between coffinite and stetindite, as well as the analogous trends observed in their phonon dispersion curves, the eigenmodes in stetindite were identified through a comparison with previous DFT calculations on coffinite. Specifically, modes with similar energetic order and dispersion curve shapes were identified as the same modes. However, it is worth mentioning the discrepancies in previous computational and experimental studies regarding the assignment of motional eigenmodes. For zircon $ZrSiO_4$, two different orders have been reported: $E_g^1 < B_{1g}^1 < E_g^2 < E_g^3 < B_{1g}^2$ and $E_g^1 < B_{1g}^1 < E_g^2 < A_{2g} < B_{2g}$ (Raman spectrum of synthetic zircon ($ZrSiO_4$,) and thorite ($ThSiO_4$)).[49,60] For coffinite, Li Su *et al.* indicated the energetic order $E_g^1 < B_{1g}^1 < E_g^2 < E_g^3 < B_{1g}^2$,[50] however, J. D. Bauer *et al.* showed different energetic order, $E_g^1 < B_{2g} < B_{1g}^1$.[26] The eigenvalues of the zircon modes exhibit notable distinctions compared to those of coffinite. For instance, the E_g^1 mode of zircon is twice that of coffinite. This divergence can be attributed to the substantial variation in reduced mean mass between U–O and Zr–O, as well as differences in bond strength. More research on

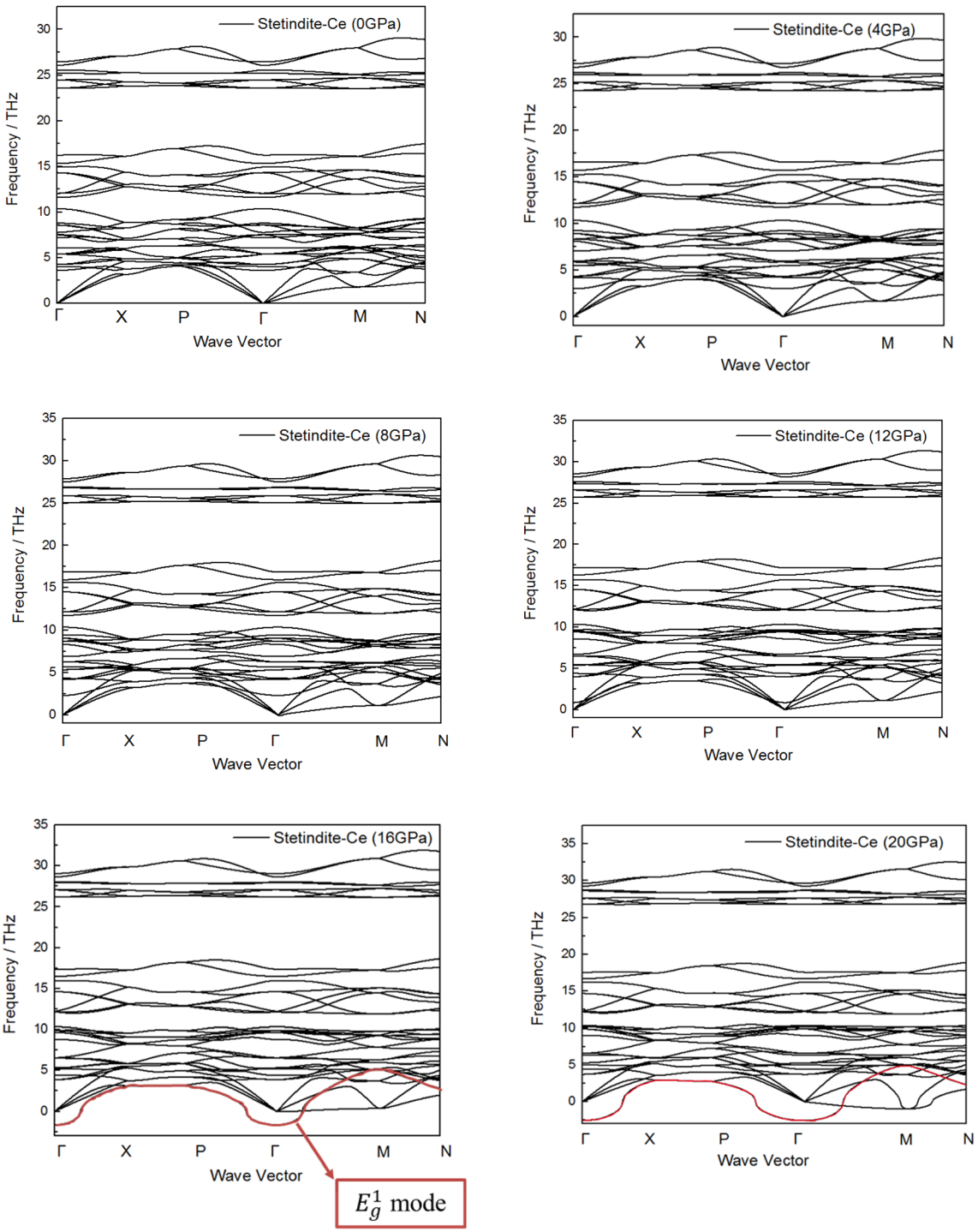

Fig. 3 Phonon dispersion spectra of stetindite $CeSiO_4$ under different pressures.

the Raman modes identification is highly recommended in the future.

The dominant mode along the compression mode is the Raman active E_g^1 rotational mode. The E_g^1 mode's softening within the stetindite structure is a critical aspect of the high-pressure phase transition. This mode's frequency changes can be indicative of structural instability. At ambient condition, the E_g^1 mode shows a frequency of 3.62 THz, with increasing pressure, the mode E_g^1 shows a softening process. Between 12 and 16 GPa, E_g^1 mode was calculated as negative values, which is a sign of the instability of the stetindite phase. In this pressure range, the stetindite structure becomes unstable, leading to significant changes in the atomic arrangements to a low symmetry mode. Based on previous synchrotron XRD

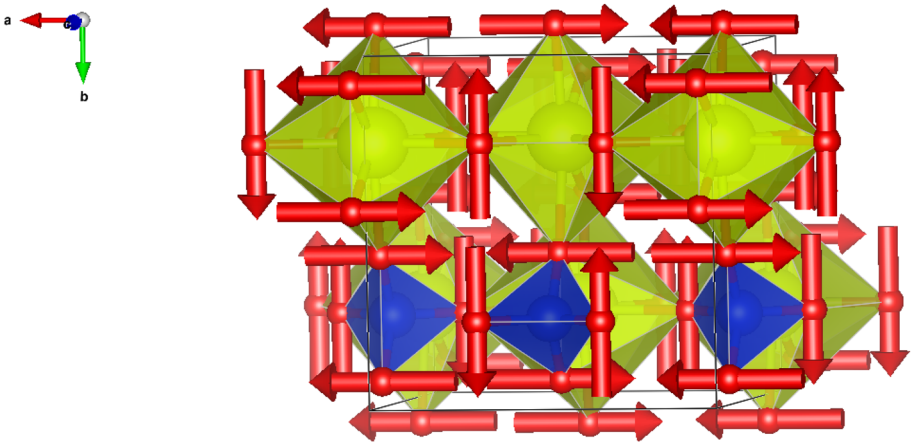

Fig. 4 Preferable motion direction representation of the E_g^1 mode.

refinement, there is a HPLS phase (space group $I\bar{4}_2d$) between the transition of stetindite and scheelite phase.[30] There is no significant difference between the volume of stetindite phase (V = 278.84(38) A^3 at ~14.49 GPa) and the volume of HPLS phase (V = 275.71(5) A^3 at ~15.09 GPa).[30] The enthalpies of the two phases became close beyond 8.35 GPa and the volume showed continuity with the intermediate HPLS phase, suggesting a gradual rather than a discontinuous transition. Combining the experimental observation and the calculations in this work, a softening-mode driven second-order phase transition could be concluded. The twist of the oxygen cage results in the loss of the symmetry element of the reflection mirror normal to the x axis and the axial glide plane type of d to [110] (as in Fig. 4), which explains the phase transformation from stetindite $I4_1/amd$ to scheelite $I4_1/a$. The E_g^1 mode has not been observed in the experiment due to the low frequency. To gain a comprehensive understanding of this intriguing phase transition, further experiments, particularly low-frequency Raman scattering studies, are strongly recommended.

Overall, the DFT calculation revealed that the softening of the E_g^1 mode is the main driving force of the phase transition instead of enthalpy, and a low symmetry intermediate phase is likely to emerge by the motion of the oxygen atoms. In future work, the oxygen atoms will be perturbated according to the eigen vectors of the E_g^1 mode, and more investigation will be done to reveal the properties of the high-pressure low-symmetry phase.

4. Conclusion

This study used a DFT+U and DFPT methodology to investigate the phase transition mechanism of $CeSiO_4$ stetindite and scheelite under high pressure. The calculated unit cell parameters and bulk moduli by the strain–stress method closely match experimental values. Notably, it was observed that the formation enthalpy of stetindite remains lower than that of scheelite until approximately 8.35 GPa. Despite the scheelite phase being more thermodynamically stable than stetindite, at around 8.35 GPa by DFT+U calculations, the lattice of stetindite phase is still stable and persists. The calculated phonon spectra by DFPT revealed the softening of the E_g^1 rotational mode, which becomes imaginary between 12 and 16 GPa, indicating lattice instability. Integrating both experimental findings with HPLS phase at ~15 GPa and computational analyses from this study, it leads to the conclusion of a second-order phase transition driven by a softening mode. The resulting twist in the oxygen cage breaks the symmetry element, leading to the transition from stetindite ($I4_1/amd$) to lower symmetry. The E_g^1 mode has not been observed experimentally due to its low frequency, highlighting the need for either further low-frequency Raman scattering or single crystal high-pressure X-ray diffraction studies. Overall, this work suggests that the phase transition of $CeSiO_4$: stetindite → scheelite is predominantly lattice dynamically driven by the softening of the E_g^1 mode, offering valuable insights into the behavior of these materials under extreme pressure conditions and laying the foundation for future research on the intermediate high-pressure low-symmetry phase.

Author contributions

Xiaofeng Guo and Liang Qi conceived the idea, provided supervision and draft revision. Xiaodong Zhao performed the calculations, analyzed the data and wrote the initial draft. Andrew C. Strzelecki and Nicolas Dacheux provided the experimental results and enrolled in the discussion of the results. All the members are enrolled in the manuscript writing and discussion.

Conflicts of interest

There are no conflicts of interest to declare.

Acknowledgements

We acknowledge the supports by the National Science Foundation (NSF), Division of Earth Sciences, under award no. 2149848, and Division of Materials Research, under award no. 2144792. This research used resources from the Center for Institutional Research Computing at Washington State University. Portions of this research were supported by the WSU-PNNL Nuclear Science and Technology Institute, and Alexandra Navrotsky Institute for Experimental Thermodynamics. Xiaodong Zhao also acknowledges Yihui Wei (University of Utah) for help of acquiring computing resource and the beneficial discussion with Micah Prange (Pacific Northwest National Laboratory).

References

1 X. Guo, S. Szenknect, A. Mesbah, S. Labs, N. Clavier, C. Poinssot, S. V. Ushakov, H. Curtius, D. Bosbach, R. C. Ewing, P. Burns, N. Dacheux and A. Navrotsky, Thermodynamics of formation of coffinite, USiO4, *Proc. Natl. Acad. Sci. U. S. A.*, 2015, **112**(21), 6551–6555.

2 R. C. Ewing, W. J. Weber and J. Lian, Nuclear waste disposal—Pyrochlore (A 2 B 2 O 7): Nuclear waste form for the immobilization of plutonium and "minor" actinides, *J. Appl. Phys.*, 2004, **95**(11), 5949–5971.

3 C. G. Whipple, Can nuclear waste be stored safely at yucca mountain?, *Sci. Am.*, 1996, **274**(6), 72–79.

4 M. I. Ojovan and S. V. Yudintsev, Glass, ceramic, and glass-crystalline matrices for HLW immobilisation, *Open Ceram.*, 2023, **14**, 100355.

5 J. Starks, *Purex process*, Du Pont de Nemours (EI) and Co., Aiken, SC (USA), Savannah River Plant, 1977.

6 R. Ewing, W. Lutze and W. J. Weber, Zircon: A host-phase for the disposal of weapons plutonium, *J. Mater. Res.*, 1995, **10**, 243–246.

7 K. L. Brown, *Plutopia: Nuclear families, atomic cities, and the great Soviet and American plutonium disasters*, Oxford University Press, USA, 2013.

8 E. Horwitz and W. Schulz, The Truex process: A vital tool for disposal of US defense nuclear waste, in *New separation chemistry techniques for radioactive waste and other specific applications*, 1991, pp. 21–29.

9 G. Choppin and A. Morgenstern, Radionuclide separations in radioactive waste disposal, *J. Radioanal. Nucl. Chem.*, 2000, **243**(1), 45–51.

10 J. S. McCloy and A. Goel, Glass-ceramics for nuclear-waste immobilization, *MRS Bull.*, 2017, **42**(3), 233–240.

11 D. Caurant, P. Loiseau, O. Majerus, V. Aubin-Chevaldonnet, I. Bardez and A. Quintas, *Glasses, glass-ceramics and ceramics for immobilization of highly radioactive nuclear wastes*, Nova Science Hauppauge, 2007.

12 C. Keller, *Untersuchungen über die Germanate und Silikate des Typs ABO4 der vierwertigen Elemente Thorium bis Americium*, Gesellschaft für Kernforschung mbh, 1963.

13 J. Speer, The actinide orthosilicates, *Rev. Mineral. Geochem.*, 1980, **5**(1), 113–135.

14 R. C. Ewing, The design and evaluation of nuclear-waste forms: clues from mineralogy, *Can. Mineral.*, 2001, **39**(3), 697–715.

15 R. C. Ewing, Nuclear waste forms for actinides, *Proc. Natl. Acad. Sci. U. S. A.*, 1999, **96**(7), 3432–3439.

16 W. J. Weber, R. C. Ewing, C. A. Angell, G. W. Arnold, A. N. Cormack, J. M. Delaye, D. L. Griscom, L. W. Hobbs, A. Navrotsky and D. L. Price, Radiation effects in glasses used for immobilization of high-level waste and plutonium disposition, *J. Mater. Res.*, 1997, **12**(8), 1948–1978.

17 A. C. Strzelecki, X. Zhao, P. Estevenon, H. Xu, N. Dacheux, R. C. Ewing and X. Guo, Crystal Chemistry and Thermodynamic Properties of Zircon Structure-Type Materials, *Am. Mineral.*, 2024, **109**, 225–242.

18 A. Migdisov, H. Nisbet, N. Li, J. White, H. Xu, A. Nelson and R. Roback, Instability of U3Si2 in pressurized water media at elevated temperatures, *Commun. Chem.*, 2021, **4**(1), 65.

19 E. N. R. Data, National Nuclear Data Center. Brookhaven National Laboratory (**https://www.nndc.bnl.gov/exfor/exfor00.htm**) and International Atomic Energy Agency, Nuclear Data Services (**https://www-nds.iaea.org/exfor/exfor.htm**) 2000.

20 A. P. Deditius, S. Utsunomiya and R. C. Ewing, The chemical stability of coffinite, $USiO4 \cdot nH_2O$; $0 < n < 2$, associated with organic matter: A case study from Grants uranium region, New Mexico, USA, *Chem. Geol.*, 2008, **251**(1–4), 33–49.

21 A. P. Deditius, S. Utsunomiya and R. C. Ewing, Alteration of Coffinite (USiO4) Under Reducing and Oxidizing Conditions, *MRS Online Proc. Libr.*, 2006, **985**, 1–6.

22 J. Janeczek and R. Ewing, Coffinitization-a mechanism for the alteration of UO2 under reducing conditions, *MRS Online Proc. Libr.*, 1991, **257**, 497.

23 S. Szenknect, A. Mesbah, T. Cordara, N. Clavier, H.-P. Brau, X. Le Goff, C. Poinssot, R. C. Ewing and N. Dacheux, First experimental determination of the solubility constant of coffinite, *Geochim. Cosmochim. Acta*, 2016, **181**, 36–53.

24 R. M. Hazen, R. C. Ewing and D. A. Sverjensky, Evolution of uranium and thorium minerals, *Am. Mineral.*, 2009, **94**(10), 1293–1311.

25 F. Zhang, V. Pointeau, L. Shuller, D. Reaman, M. Lang, Z. Liu, J. Hu, W. Panero, U. Becker and C. Poinssot, Structural transitions and electron transfer in coffinite, USiO4, at high pressure, *Am. Mineral.*, 2009, **94**(7), 916–920.

26 J. Bauer, S. Labs, S. Weiss, L. Bayarjargal, W. Morgenroth, V. Milman, A. Perlov, H. Curtius, D. Bosbach and H. Zänker, High-pressure phase transition of coffinite, USiO4, *J. Phys. Chem. C*, 2014, **118**(43), 25141–25149.

27 A. C. Strzelecki, T. Barral, P. Estevenon, A. Mesbah, V. Goncharov, J. Baker, J. Bai, N. Clavier, S. Szenknect, A. Migdisov, H. Xu, R. C. Ewing, N. Dacheux and X. Guo, The role of water and hydroxyl groups in the structures of

stetindite and coffinite, MSiO4 (M = Ce, U), *Inorg. Chem.*, 2021, **60**(2), 718–735.
28 T. Barral, P. Estevenon, Y. Chanteau, T. Kaczmarek, A. C. Strzelecki, D. Menut, E. Welcomme, S. Szenknect, P. Moisy, X. Guo and N. Dacheux, How hydrothermal synthesis improves the synthesis of (Zr, Ce) SiO 4 solid solutions, *Dalton Trans.*, 2023, **52**(29), 10023–10037.
29 E. Ferriss, R. Ewing and U. Becker, Simulation of thermodynamic mixing properties of actinide-containing zircon solid solutions, *Am. Mineral.*, 2010, **95**(2–3), 229–241.
30 A. C. Strzelecki, X. Zhao, J. L. Baker, P. Estevenon, T. Barral, A. Mesbah, D. Popov, S. Chariton, V. Prakapenka, S. Ahmed, C. Yoo, N. Dacheux, H. Xu and X. Guo, High-pressure structural and thermodynamic properties of cerium orthosilicates (CeSiO4), *J. Phys. Chem. C*, 2023, **127**(8), 4225–4238.
31 A. C. Strzelecki, C. Bourgeois, K. W. Kriegsman, P. Estevenon, N. Wei, S. Szenknect, A. Mesbah, D. Wu, R. C. Ewing, N. Dacheux and X. Guo, Thermodynamics of CeSiO4: implications for actinide orthosilicates, *Inorg. Chem.*, 2020, **59**(18), 13174–13183.
32 P. Estevenon, E. Welcomme, C. Tamain, G. Jouan, S. Szenknect, A. Mesbah, C. Poinssot, P. Moisy and N. Dacheux, The formation of PuSiO 4 under hydrothermal conditions, *Dalton Trans.*, 2020, **49**(19), 6434–6445.
33 P. Estevenon, E. Welcomme, S. Szenknect, A. Mesbah, P. Moisy, C. Poinssot and N. Dacheux, Study of the hydrothermal synthesis of ThSiO4, USiO4 and CeSiO4 aiming at determining the conditions of PuSiO4 formation. In 2017 E-MRS Fall Meeting, 2017.
34 H. Xu and Y. Wang, Prediction of thermodynamic property of Pu-zircon and Pu-pyrochlore, In AIP Conference Proceedings, 2000, AIP Publishing: Vol. 532, pp. 363–363.
35 N. Dacheux, P. Estevenon, A. C. Strzelecki, S. Szenknect, P. Moisy, R. Ewing, X. Guo and A. Navrotsky, Formation of CeSiO4 and AnSiO4 (An=Th, U, Pu): insights coming from hydrothermal synthesis and thermodynamic issues. In Goldschmidt 2023 Conference, 2023; GOLDSCHMIDT.
36 B. Mihailova, N. Waeselmann, C. Stangarone, R. J. Angel, M. Prencipe and M. Alvaro, The pressure-induced phase transition (s) of ZrSiO _4 ZrSiO 4: revised: Experimental proof for the existence of a new high-pressure polymorph of zircon, *Phys. Chem. Miner.*, 2019, **46**, 807–814.
37 G. Kresse and J. Furthmüller, Efficiency of ab initio total energy calculations for metals and semiconductors using a plane-wave basis set, *Comput. Mater. Sci.*, 1996, **6**(1), 15–50, DOI: 10.1016/0927-0256(96)00008-0.
38 G. Kresse and J. Furthmüller, Software VASP, vienna (1999), *Phys. Rev. B: Condens. Matter Mater. Phys.*, 1996, **54**(11), 169.
39 G. Kresse and J. Hafner, Ab initio molecular dynamics for liquid metals, *Phys. Rev. B: Condens. Matter Mater. Phys.*, 1993, **47**(1), 558.
40 G. Kresse, Comput. matter sci. 6, 15 (1996);(d) kresse, g., and furthmuller, *Phys. Rev. B: Condens. Matter Mater. Phys.*, 1996, **54**, 11–169.
41 P. E. Blöchl, Projector augmented-wave method, *Phys. Rev. B: Condens. Matter Mater. Phys.*, 1994, **50**(24), 17953–17979, DOI: 10.1103/PhysRevB.50.17953.
42 G. Kresse and D. Joubert, From ultrasoft pseudopotentials to the projector augmented-wave method, *Phys. Rev. B: Condens. Matter Mater. Phys.*, 1999, **59**(3), 1758–1775, DOI: 10.1103/PhysRevB.59.1758.
43 A. A. Emery and C. Wolverton, High-Throughput DFT calculations of formation energy, stability and oxygen vacancy formation energy of ABO 3 perovskites, *Sci. Data*, 2017, **4**, 170153.
44 S. Baroni, S. De Gironcoli, A. Dal Corso and P. Giannozzi, Phonons and related crystal properties from density-functional perturbation theory, *Rev. Mod. Phys.*, 2001, **73**(2), 515.
45 A. Togo, L. Chaput, T. Tadano and I. Tanaka, Implementation strategies in phonopy and phono3py, *J. Phys.: Condens. Matter*, 2023, **35**, 353001.
46 A. Togo, First-principles phonon calculations with phonopy and phono3py, *J. Phys. Soc. Jpn.*, 2023, **92**(1), 012001.
47 A. Togo and I. Tanaka, First principles phonon calculations in materials science, *Scr. Mater.*, 2015, **108**, 1–5.
48 M. I. Aroyo, J. M. Perez-Mato, C. Capillas, E. Kroumova, S. Ivantchev, G. Madariaga, A. Kirov and H. Wondratschek, Bilbao Crystallographic Server: I. Databases and crystallographic computing programs, *Z. Kristallogr. - Cryst. Mater.*, 2006, **221**(1), 15–27.
49 R. Syme, D. Lockwood and H. Kerr, Raman spectrum of synthetic zircon (ZrSiO4) and thorite (ThSiO4), *J. Phys. C: Solid State Phys.*, 1977, **10**(8), 1335.
50 L. Su, L. Wan, T. Gao and B. Ao, First-principles calculations of the electronic structure, chemical bonding, and thermodynamic properties of USiO4, *AIP Adv.*, 2020, **10**(7), 075018.
51 Z. Li and S. T. John, Phonon anomaly in high-pressure Zn, *Phys. Rev. Lett.*, 2000, **85**(24), 5130.
52 K. Parlinski and Y. Kawazoe, Ab initio study of phonons in the rutile structure of under pressure, *Eur. Phys. J. B*, 2000, **13**(4), 679–683.
53 A. R. Albuquerque, J. Maul, E. Longo, I. M. Dos Santos and J. R. Sambrano, Hydrostatic and [001] uniaxial pressure on anatase TiO2 by periodic B3LYP-D* calculations, *J. Phys. Chem. C*, 2013, **117**(14), 7050–7061.
54 G. Kresse, VASP the Guide. https://cms.mpi.univie.ac.at/vasp/, 2001.
55 L. Tian, *Density Functional Study of Elastic Properties of Metallic Alloys*. KTH Royal Institute of Technology, 2015.
56 K. Doll, Analytical stress tensor and pressure calculations with the CRYSTAL code, *Mol. Phys.*, 2010, **108**(3–4), 223–227.
57 V. Weber, C. J. Tymczak and M. Challacombe, Energy gradients with respect to atomic positions and cell parameters for the Kohn-Sham density-functional theory at the Γ point, *J. Chem. Phys.*, 2006, **124**(22), 224107.
58 J.-P. Poirier and A. Tarantola, A logarithmic equation of state, *Phys. Earth Planet. Inter.*, 1998, **109**(1–2), 1–8.

59 J. Gonzalez-Platas, M. Alvaro, F. Nestola and R. Angel, EosFit7-GUI: a new graphical user interface for equation of state calculations, analyses and teaching, *J. Appl. Crystallogr.*, 2016, **49**(4), 1377–1382.
60 C. Stangarone, R. J. Angel, M. Prencipe, N. Campomenosi, B. Mihailova and M. Alvaro, Measurement of strains in zircon inclusions by Raman spectroscopy, *Eur. J. Mineral.*, 2019, **31**(4), 685–694.
61 T. Geisler, B. E. Burakov, V. Zirlin, L. Nikolaeva and P. PöML, A Raman spectroscopic study of high-uranium zircon from the Chernobyl "lava", *Eur. J. Mineral.*, 2005, **17**(6), 883–894.
62 N. Clavier, S. Szenknect, D. Costin, A. Mesbah, C. Poinssot and N. Dacheux, From thorite to coffinite: A spectroscopic study of Th1− xUxSiO4 solid solutions, *Spectrochim. Acta, Part A*, 2014, **118**, 302–307.